

# Journal of Biomedical Optics

[SPIEDigitalLibrary.org/jbo](http://SPIEDigitalLibrary.org/jbo)

## **Investigation of the hyper-reflective inner/outer segment band in optical coherence tomography of living frog retina**

Rong-Wen Lu  
Christine A. Curcio  
Youwen Zhang  
Qiu-Xiang Zhang  
Steven J. Pittler  
Dusanka Deretic  
Xin-Cheng Yao

# Investigation of the hyper-reflective inner/outer segment band in optical coherence tomography of living frog retina

Rong-Wen Lu,<sup>a</sup> Christine A. Curcio,<sup>b</sup> Youwen Zhang,<sup>c</sup> Qiu-Xiang Zhang,<sup>a</sup> Steven J. Pittler,<sup>c</sup> Dusanka Deretic,<sup>d</sup> and Xin-Cheng Yao<sup>a,c</sup>

<sup>a</sup>University of Alabama at Birmingham, Department of Biomedical Engineering, Birmingham, Alabama 35294

<sup>b</sup>University of Alabama at Birmingham, Department of Ophthalmology, Birmingham, Alabama 35294

<sup>c</sup>University of Alabama at Birmingham, Department of Vision Sciences, Birmingham, Alabama 35294

<sup>d</sup>University of New Mexico, Department of Surgery, Division of Ophthalmology, Albuquerque, New Mexico 87131

**Abstract.** This study is to test anatomic correlates, including connecting cilium (CC) and inner segment (IS) ellipsoid, to the hyper-reflective band visualized by optical coherence tomography (OCT) and commonly attributed to the photoreceptor inner/outer segment (IS/OS) junction. A line-scan OCT (LS-OCT) was constructed to achieve sub-cellular resolution (lateral:  $\sim 2 \mu\text{m}$ ; axial:  $\sim 4 \mu\text{m}$ ) of excised living frog retinas. An electro-optic phase modulator was employed for rapid and vibration-free phase modulation. Comparison of normalized distance measurements between LS-OCT images and histological images revealed that the dominant source of the signal reported as the IS/OS OCT band actually originates from the IS. © 2012 Society of Photo-Optical Instrumentation Engineers (SPIE). [DOI: [10.1117/1.JBO.17.6.060504](https://doi.org/10.1117/1.JBO.17.6.060504)]

Keywords: retina; optical coherence tomography; photoreceptor; inner segment; outer segment.

Paper 12199L received Mar. 27, 2012; revised manuscript received Apr. 24, 2012; accepted for publication Apr. 27, 2012; published online Jun. 6, 2012.

Given the excellent capability to identify morphological changes at individual functional layers of the retina, optical coherence tomography (OCT) has an increasing application in eye disease detection.<sup>1</sup> In-depth understanding of anatomic sources of the OCT signal is essential for accurate interpretation of clinical outcomes, and is valuable for instrument optimization to improve imaging sensitivity and selectivity. Early studies have disclosed four hyper-reflective OCT bands at the outer retina, i.e., photoreceptor side. Anatomic sources of these four OCT bands have been typically attributed as follows: first (1st) band at the outer limiting membrane (OLM); second (2nd) band at the photoreceptor inner/outer-segment (IS/OS)

junction; third (3rd) band at the posterior tip of the OS; and fourth (4th) band at the retinal pigment epithelium (RPE).<sup>2</sup> Anatomic correlates of the 2nd band remains controversial. The 2nd OCT band is widely attributed to the IS/OS junction, which cell biologists consider the connecting cilium (CC) between these structures. However, comparative alignment of OCT bands with an anatomically correct model of the outer retina suggested an alternative correlate, i.e., the IS ellipsoid,<sup>3</sup> to the 2nd OCT band. Previous investigation has indicated that the physiological condition may affect the 2nd OCT band recording.<sup>4</sup> Therefore, freshly isolated living retinas were used for OCT imaging.

Leopard (*Rana pipiens*) frog was selected for this study. Large photoreceptors (cone:  $\sim 3 \mu\text{m}$  and rod:  $\sim 6 \mu\text{m}$ )<sup>5</sup> of the frog enabled accurate OCT recording at sub-cellular resolution. The experimental procedures were approved by the Institutional Animal Care and Use Committee of the University of Alabama at Birmingham. Without complications of ocular aberrations and signal contamination of other ocular tissues, isolated retinas provided a simple preparation to allow high resolution OCT characterization of the retina. Details of the preparation procedures of freshly isolated living retinas, which have been used to investigate stimulus-evoked retinal neural activities, have been previously reported.<sup>6,7</sup> During the OCT imaging, the isolated retina was immersed in oxygenated Ringer's solution to maintain its viability.

In order to achieve sub-cellular resolution in both lateral and axial directions, a rapid line-scan OCT (LS-OCT) was developed. The LS-OCT combined technical merits of our recently demonstrated electro-optic phase modulator (EOPM) based functional OCT<sup>6</sup> and line-scan confocal microscopy.<sup>7</sup> Figure 1 shows a simplified diagram of the LS-OCT. In this system, a near infrared superluminescent laser diode (SLD-35-HP, Superlum) with center wavelength  $\lambda = 830 \text{ nm}$  and bandwidth  $\Delta\lambda = 60 \text{ nm}$  was used for light illumination. A water immersion objective (10 $\times$ , NA = 0.3) was applied for OCT imaging. The lateral resolution of the system was estimated at  $\sim 2 \mu\text{m}$  ( $0.61\lambda/\text{NA}$ ), and the axial resolution of the LS-OCT was  $\sim 4 \mu\text{m}$  ( $0.44\lambda^2/n\Delta\lambda$ , where refractive index  $n$  of the sample was assumed  $\sim 1.4$ ). Using a mirror immersed in water solution, the actual axial resolution was experimentally measured at  $\sim 5 \mu\text{m}$ .

In the illumination path [optics above the beam splitter BS, Fig. 1(a)], a cylindrical lens CL1 was employed to condense the collimated SLD light in one dimension to produce a focused line illumination which was imaged at the retina through lenses L3, L4, L5, and the objective OB. The long axis of the focused line was parallel to the  $y$ -axis in the OCT image [Fig. 2(a)]. The active area of the high-speed (70,000 lines/s) linear camera (spL2048-140k, Basler Sprint) was conjugated to the focused line illumination. The line-sensor ( $1 \times 2048$  pixels,  $10 \times 10 \mu\text{m}^2$ ) of the linear camera naturally acted as a spatial-filter to reject out-of-focus light. Thus, a LS confocal mechanism was achieved to reduce background light and therefore maximize effective OCT contrast and dynamic range.

In the reference path [optics below the BS, Fig. 1(a)], another cylindrical lens CL2 was used to convert the focused light back to a collimated light beam before entering the EOPM (Model 350-50, Conoptics) that was used to generate rapid vibration- and inertia-free phase modulation.<sup>6</sup> A four-step phase-shifting strategy was employed to retrieve OCT images.<sup>8</sup> The glass

Address all correspondence to: Xin-Cheng Yao, University of Alabama at Birmingham, Department of Biomedical Engineering, Birmingham, Alabama 35294. Tel.: +205 9967459; Fax: +205 9343425; E-mail: [xcy@uab.edu](mailto:xcy@uab.edu)

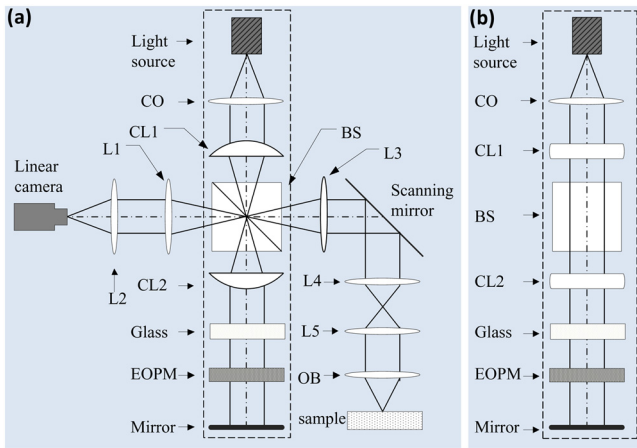


**Fig. 1** (a) Schematic diagram of the LS-OCT. BS: beam splitter; CO: collimator; L1 ~ L5: lenses; OB: objective; CL1 and CL2: cylindrical lenses. The focal length of CL1, CL2, L1 ~ L5 was 40, 40, 40, 80, 80, 40, and 75, respectively. (b) The side view of the optical geometry of the illumination and reference paths (dashed square in a).

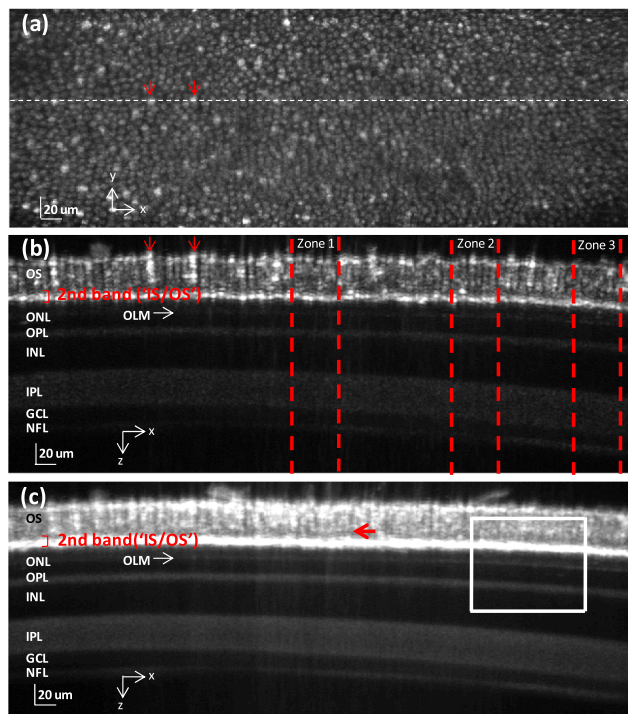
block in the reference arm was used to compensate for optical dispersion of the sample beam. Figure 1(b) shows side view of the illumination and reference paths [dashed square in Fig. 1(a)]. In the side view, the cylindrical lenses CL1 and CL2 acted as a pair of glass plates.

Our custom-designed LS-OCT provided both en-face and B-scan recording capabilities. The galvo scanning mirror (GVS001, Thorlabs) could provide rapid en-face [Fig. 2(a)]

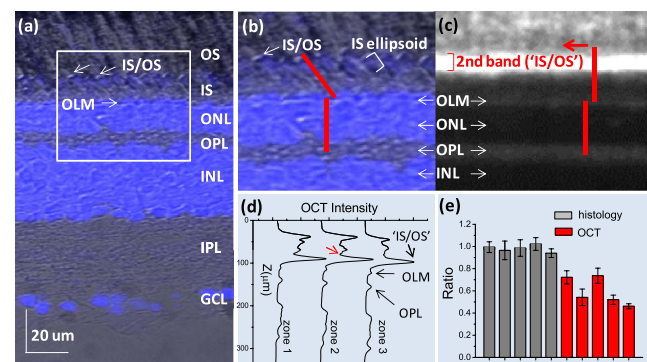
imaging up to 400 Hz; while the motorized sample platform (Z825B, Thorlabs) could scan in the z-direction to achieve B-scan recording [Fig. 2(b)] of the cross-section of flat-mount retinas.

Figure 2 shows representative en-face and B-scan OCT images of isolated retina in which the retinal pigment epithelium (RPE) was not included. During the recording, the photoreceptors were upward, i.e., facing to the objective, to improve image quality of the outer retina. Given the sub-cellular resolution, the en-face image [Fig. 2(a)] revealed individual photoreceptors. B-scan image [Fig. 2(b)] disclosed individual layers from the photoreceptor to inner retina. After adapting band nomenclature used in high resolution OCT of human retina to frog retina,<sup>2</sup> we labeled individual layers. As shown in Fig. 2(b), the OS, 'IS/OS' (presumed), OLM, OPL, inner plexiform layer (IPL), and nerve fiber layer (NFL) were hyper-reflective; while the outer nuclear layer (ONL), inner nuclear layer (INL), and ganglion cell layer (GCL) were hypo-reflective. The bright 'IS/OS' band was bumpy in the high resolution OCT image. In order to achieve better visualization of individual OCT bands, Fig. 2(c) shows an averaged cross-section image over 120  $\mu\text{m}$  (200 B-scan images, with 0.6  $\mu\text{m}$  recording interval) along the y-axis. We consistently observed that the whole OS section, not only the OS tip or the 'IS/OS' junction, produced OCT signal; and the band of lower reflectivity [red arrow in Fig. 2(c)] was observed located sclerally to the 2nd OCT band. Moreover, bright spots [red arrows in Fig. 2(a) and 2(b)], with dimension at cellular level, were consistently observed. This might reflect reflectance inhomogeneity of different photoreceptors in the frog retina that has two types each of cones and rods.

Figure 3 shows comparative histological [Fig. 3(a) and 3(b)] and LS-OCT [Fig. 3(c)] images. For histological examination, DNA was stained with DAPI (blue) with Prolong Gold antifade mounting reagent (Invitrogen) in 10- $\mu\text{m}$  thick fixed retinal cryosections.<sup>9</sup> The DNA marked fluorescence image and the differential interference contrast (DIC) image were superimposed. Based on previously reported light<sup>10</sup> and electron<sup>5</sup>



**Fig. 2** LS-OCT images. (a) En-face image of OS, acquired by averaging a stack of images of OS over 20  $\mu\text{m}$ . (b) Cross-section OCT image of the area marked by the white dashed line in a. Zones 1 to 3 marked by vertical lines were used for quantitative analysis in Fig. 3(d). (c) Cross-section OCT image averaged over 120  $\mu\text{m}$  along the y-axis. The intensity was multiplied by 2, compared to the image in b. Red arrow points to a local hypo-reflective band. The white window shows the area for enlarged display in Fig. 3(c).



**Fig. 3** (a) Histological image. (b) Enlarged sub-image marked by the white window in (a). (c) Enlarged image of OCT sub-image marked by the white window in (b) and (c). Four red bars in (b) and (c) have identical length. (d) Curves of OCT intensity over retinal depth (z axis) of three zones in Fig. 2(b). The red arrow points to the local hypo-reflective band, bordering posteriorly on the 'IS/OS' band [red arrows in Figs. 2(c) and 3(c)]. (e) Histological distance ratio  $(H_{IS/OS} - H_{OLM}) / (H_{OLM} - H_{OPL})$  and the OCT distance ratio  $(OCT_{IS/OS} - OCT_{OLM}) / (OCT_{OLM} - OCT_{OPL})$ . Five samples were used for histological and OCT measurements, respectively. For each sample, six positions were measured. Error bars indicate standard deviations.

microscopy investigations of frog retinas, the IS/OS, OLM, OPL, etc. were identified in Fig. 3(a). For the frog retina, the ONL could be identified as having two rows of nuclei.<sup>5,10</sup> Frog IS ellipsoid, like humans, is full of mitochondria<sup>3,5</sup> that contains DNA. Therefore, IS ellipsoid portion was also stained by DAPI, and thus could be separated from other IS portions.

Figure 3(b) and 3(c) show enlarged sub-images of the histological [Fig. 3(a)] and OCT [Fig. 2(c)] images. If the 2nd OCT band is correctly attributed to the IS/OS, it would be expected to align with an anatomic counterpart in the histological image [Fig. 3(b)]. However, the center of the 2nd OCT band shifted toward to the IS, mostly like the IS ellipsoid portion. In contrast, the local hypo-reflective band [red arrow in Fig. 3(c)] might relate to the IS/OS junction.<sup>3</sup>

In order to achieve quantitative analysis, the distance between the well-established OLM and OPL bands were used to normalize the axial position of the 2nd OCT band. Figure 3(d) shows 3 representative OCT longitudinal reflectance profiles (LRPs) as a function of retinal depth for three zones specified in Fig. 2(b). Each zone was averaged over 50  $\mu\text{m}$  along the  $x$ -axis to improve signal-to-noise ratio. In theory, the OCT bands could be widened due to the logarithmic transformation or gamma correction of OCT displaying.<sup>3</sup> However, neither the logarithmic transformation nor gamma correction shifts the peaks. Therefore, the positions on the  $z$ -axis of peaks of the 'IS/OS' (2nd) band, the OLM (1st) band and the OPL band could be defined as their axial positions. Thus, OCT distance ratio  $(\text{OCT}_{\text{IS/OS}} - \text{OCT}_{\text{OLM}}) / (\text{OCT}_{\text{OLM}} - \text{OCT}_{\text{OPL}})$  could be quantitatively computed and compared to histological distance ratio of  $(H_{\text{IS/OS}} - H_{\text{OLM}}) / (H_{\text{OLM}} - H_{\text{OPL}})$ .

Figure 3(e) shows statistics of OCT and histological distance ratios. Five retinas were used for OCT imaging, and corresponding five retinas were used for histology measurement. For each sample, six lateral positions were measured for estimating the distance ratio. As shown in Fig. 3(e), the histological distance ratio of  $(H_{\text{IS/OS}} - H_{\text{OLM}}) / (H_{\text{OLM}} - H_{\text{OPL}})$  was  $1.0 \pm 0.05$ . In contrast, the mean of  $(\text{OCT}_{\text{IS/OS}} - \text{OCT}_{\text{OLM}}) / (\text{OCT}_{\text{OLM}} - \text{OCT}_{\text{OPL}})$  was  $0.6 \pm 0.1$ . The significant difference ( $t$ -test,  $p < 0.003$ ) between the  $(\text{OCT}_{\text{IS/OS}} - \text{OCT}_{\text{OLM}}) / (\text{OCT}_{\text{OLM}} - \text{OCT}_{\text{OPL}})$  and  $(H_{\text{IS/OS}} - H_{\text{OLM}}) / (H_{\text{OLM}} - H_{\text{OPL}})$  suggested that the 2nd OCT band might not actually relate to the IS/OS junction.

In summary, a LS-OCT was developed to demonstrate OCT imaging at sub-cellular resolution in both lateral [Fig. 2(a)] and axial [Fig. 2(b)] directions. Quantitative comparison of histological images and LS-OCT images revealed that the OCT distance ratio  $(\text{OCT}_{\text{IS/OS}} - \text{OCT}_{\text{OLM}}) / (\text{OCT}_{\text{OLM}} - \text{OCT}_{\text{OPL}})$  was significantly smaller than the histological distance ratio  $(H_{\text{IS/OS}} - H_{\text{OLM}}) / (H_{\text{OLM}} - H_{\text{OPL}})$ . The significant difference suggests that dominant source of the signal reported as the 'IS/OS' OCT band actually originates from the IS. We speculate that the IS ellipsoid, which consists of abundant mitochondria, or the CC extended into the IS<sup>11</sup> may contribute to the observed 2nd OCT band signal.

Moreover, reflectance inhomogeneity was consistently observed at cellular level [Fig. 2(a) and 2(b)]. The bumpy 2nd OCT band shown in Fig. 2b might attribute to variable lengths and axial locations of different rod/cone photoreceptors.<sup>5</sup> Robust OCT signal was observed through the whole length of the photoreceptor outer segment. Early

spectral-domain OCT study (SD-OCT) did not report OCT signal in the outer segment, i.e., the depth between the presumed 'IS/OS' band and the posterior tip of the OS.<sup>2</sup> We speculate that this discrepancy might attribute to large (0.3) numeric aperture (NA) of the LS-OCT system, compared to  $\sim 0.1$  NA in typical SD-OCT system for retinal imaging. Increased NA could improve collection efficiency of reflected light, particularly scattering light with possible large angle changes, relative to incident light, from outer segment discs. In addition, the large NA system might produce illumination light with incident angle greater than the optimized acceptance of the photoreceptor, which acted as a waveguide.<sup>12</sup> Therefore, more light might be scattered and thus detected from the OS. We expect that further characterization of these observed OCT signals will provide insight for improved instrumental design, validated image attribution, and retinal diagnosis.

### Acknowledgments

The authors thank Jerry Millican and Yangguo Li for mechanical fabrication and prototype construction of the LS-OCT. This research is supported partially by Dana Foundation (Brain and Immuno-Imaging Grant program); Eyesight Foundation of Alabama, NSF CBET-1055889, NIH R21 RR025788, NIH R21 EB012264, NIH R01 EY06109, NIH R01 EY018143 and Vision Sciences Core grant NIH P30 EY03039.

### References

1. D. C. Hood et al., "The inner segment/outer segment border seen on optical coherence tomography is less intense in patients with diminished cone function," *Invest. Ophthalmol. Vis. Sci.* **52**(13), 9703–9709 (2011).
2. D. T. Miller et al., "Adaptive optics and the eye (super resolution OCT)," *Eye (Lond)* **25**(3), 321–330 (2011).
3. R. F. Spaide and C. A. Curcio, "Anatomical correlates to the bands seen in the outer retina by optical coherence tomography: literature review and model," *Retina* **31**(8), 1609–1619 (2011).
4. Y. Yamauchi et al., "Biological activity is the likely origin of the intersection between the photoreceptor inner and outer segments of the rat retina as determined by optical coherence tomography," *Clin. Ophthalmol.* **5**, 1649–1653 (2011).
5. S. E. Nilsson, "An electron microscopic classification of the retinal receptors of the leopard frog (*Rana pipiens*)," *J. Ultrastruct. Res.* **10**(5–6), 390–416 (1964).
6. X. C. Yao et al., "Rapid optical coherence tomography and recording functional scattering changes from activated frog retina," *Appl. Opt.* **44**(11), 2019–2023 (2005).
7. Y. G. Li et al., "High-speed line-scan confocal imaging of stimulus-evoked intrinsic optical signals in the retina," *Opt. Lett.* **35**(3), 426–428 (2010).
8. J. M. Huntley, G. H. Kaufmann, and D. Kerr, "Phase-shifted dynamic speckle pattern interferometry at 1 kHz," *Appl. Opt.* **38**(31), 6556–6563 (1999).
9. Y. Zhang et al., "Knockout of GARPs and the beta-subunit of the rod cGMP-gated channel disrupts disk morphogenesis and rod outer segment structural integrity," *J. Cell Sci.* **122**(8), 1192–1200 (2009).
10. J. Mazelova et al., "Syntaxin 3 and SNAP-25 pairing, regulated by omega-3 docosahexaenoic acid, controls the delivery of rhodopsin for the biogenesis of cilia-derived sensory organelles, the rod outer segments," *J. Cell Sci.* **122**(12), 2003–2013 (2009).
11. Q. Liu et al., "The proteome of the mouse photoreceptor sensory cilium complex," *Mol. Cell Proteomics* **6**(8), 1299–1317 (2007).
12. W. Gao et al., "Measuring retinal contributions to the optical Stiles-Crawford effect with optical coherence tomography," *Opt. Express* **16**(9), 6486–6501 (2008).